J. Fluid Mech. (2008), *vol.* 601, *pp.* 253–279. © 2008 Cambridge University Press
doi:10.1017/S0022112008000670 Printed in the United Kingdom

Vapour bubble collapse in isothermal and non-isothermal liquids

BINZE YANG[1] AND ANDREA PROSPERETTI[1,2]†

[1]Department of Mechanical Engineering, The Johns Hopkins University, Baltimore, MD 21218, USA
[2]Faculty of Applied Science and Burgerscentrum, University of Twente, AE 7500 Enschede, The Netherlands

(Received 30 November 2006 and in revised form 8 January 2008)

The motion of a vapour bubble in a subcooled liquid is studied numerically assuming axial symmetry but allowing the surface to deform under the action of the fluid dynamic stress. The flattening of the bubble in the plane orthogonal to the translational velocity increases the added mass and slows it down, while, at the same time, the decreasing volume tends to increase the velocity. The deformation of the interface also increases the surface area exposed to the incoming cooler liquid. The competition among these opposing processes is subtle and the details of the condensation cannot be captured by simpler models, two of which are considered. In spite of these differences, the estimate of the total collapse time given by a spherical model is close to that of the deforming bubble model for the cases studied. In addition to an isothermal liquid, some examples in which the bubble encounters warmer and colder liquid regions are shown.

1. Introduction

Vapour bubbles are labile entities: a small ambient pressure increase or the chance encounter with a slightly subcooled liquid eddy are likely to cause a rapid condensation of the vapour and the disappearance of the bubble on a millisecond time scale. Since these phenomena ultimately rely on heat transfer at the bubble surface, they are strongly affected by convection. In turn, the bubble velocity depends on added mass and drag, which are affected by the bubble shape, which depends on the rate of volume change and the velocity itself. It is the complex interplay among these mechanical and thermal factors which ultimately determines the bubble's fate and renders the quantitative description of bubble evolution a matter of some complexity.

Until fairly recently, all the work on translating vapour bubbles essentially relied on the assumption of negligible shape distortion (see e.g. Wittke & Chao 1967; Moalem & Sideman 1973; Gumerov 1996; Hao & Prosperetti 2000). The study of Legendre, Borée & Magnaudet (1998) is a recent example of an accurate analysis of this type and provides an excellent summary of the earlier work. More recently, thanks to the development of numerical techniques capable of dealing with this complex free-surface problem, the sphericity assumption has begun to be relaxed. Cao & Christensen (2000) approximated the bubble shape by combining two oblate half-spheroids joined along their maximum circle and used a boundary-fitted coordinate method to study the condensation of a bubble in a binary solution. In a series of

† Author to whom correspondence should be addressed: prosperetti@jhu.edu.

https://doi.org/10.1017/S0022112008000670 Published online by Cambridge University Press

papers, Li, Yan and coworkers have studied the flow and transfer phenomena around a deformable bubble of fixed volume (see e.g. Li & Yan 2002; Li, Yan & Smith 2003*b*; Li, Yan & Hull 2003*a*). Rather than solving the full Navier–Stokes equations, Szeri, *et al.* (2003) adopted a potential approximation and used a boundary integral method to calculate the flow. The work of Ye, Shyy & Chung (2003) demonstrates the power achieved by computational methods, but its tests have been limited to bubble growth rather than collapse. The same remark applies to the work of Dhir and coworkers (see e.g. Son & Dhir 1997; Son, Ramanujapu & Dhir 2002; Mukherjee & Dhir 2004).

In this paper we apply a newly developed numerical method for axisymmetric free-surface simulations (Yang & Prosperetti 2006) to study several examples of the collapse of an initially spherical vapour bubble in a subcooled liquid. In addition to an isothermal liquid, we also consider a few examples in which the bubble encounters liquid regions at different temperatures, both below and above saturation.

The main purpose of our study is the investigation of the complex interplay of the phenomena alluded to at the beginning of this section, which acquire particular relevance in microgravity conditions, where an imposed flow is often the most effective means available for bubble management. We also believe that, in view of the contemporary intense interest in the development of computational methods for free-surface flows (see e.g. Scardovelli & Zaleski 1999; Osher & Fedkiw 2001; Udaykumar *et al.* 2001; Francois & Shyy 2003; Scardovelli & Zaleski 2003; Raad & R. 2005; Shirani, Ashgriz & Mostaghimi 2005), it is useful to produce solutions that explore the parameter space and can be a helpful guide in the development and validation of more complex fully three-dimensional codes.

2. Physical considerations

A rather crude estimate of the collapse time of a stationary spherical vapour bubble was derived by Florschuetz & Chao (1965) by balancing the rate at which latent heat is liberated at the bubble surface with the rate at which it can be conducted away through the thermal boundary layer in the liquid:

$$L\rho_v \frac{\mathrm{d}}{\mathrm{d}t}\left(\frac{4}{3}\pi R^3\right) \simeq -4\pi R^2 k \frac{T_{sat}-T_\infty}{\sqrt{\pi\alpha t}}, \tag{2.1}$$

Here L is the latent heat, ρ_v the vapour density, R the bubble radius, k and α the liquid thermal conductivity and diffusivity respectively, and T_∞ the undisturbed liquid temperature far from the bubble. In writing this relation, Florschuetz & Chao (1965) assumed that the bubble surface temperature remains fixed at the saturation level T_{sat} corresponding to the ambient pressure p_∞. Upon integration from the initial radius $R(0)$ to $R=0$, they estimated the total collapse time t_c as

$$t_c = \frac{\pi}{4Ja^2}\frac{R^2(0)}{\alpha}, \tag{2.2}$$

in which the Jacob number is defined by

$$Ja = \frac{\rho c_p (T_{sat}-T_\infty)}{L\rho_v} \tag{2.3}$$

with ρ and c_p the liquid density and specific heat. This quantity may be seen as the ratio of the energy necessary to raise the temperature of the liquid from T_∞ to T_{sat} to the energy released by the condensation of vapour. For water at 100 °C, $\rho c_p/(L\rho_v) \simeq 3.0\,\mathrm{K}^{-1}$.

https://doi.org/10.1017/S0022112008000670 Published online by Cambridge University Press

In the case of a translating and condensing bubble, heat removal from the bubble surface is greatly enhanced by convection and the collapse time will be considerably shorter than the estimate (2.2).

Levich (1962) and Ruckenstein (1959) estimated the heat transfer from a translating spherical vapour bubble of constant radius by focusing on the front of the bubble and neglecting the heat transfer in the wake. They found the following result for the Nusselt number:

$$Nu \equiv \frac{2Rh}{k} = 2\sqrt{\frac{Pe}{\pi}}, \tag{2.4}$$

where h is the mean heat transfer coefficient and Pe is the Péclet number defined by

$$Pe = \frac{2RU}{\alpha} \tag{2.5}$$

with U the translational velocity of the bubble. This result has been confirmed for growing bubbles by Legendre *et al.* (1998) when $(\mathrm{d}R/\mathrm{d}t)/U$ is smaller than 1. For bubble collapse, these authors quote the expression

$$Nu \simeq 0.7\, Pe^{0.55} \tag{2.6}$$

as a good fit to their result.

With the neglect of gravity, the velocity of a bubble of negligible mass in rectilinear translation through a liquid is determined by the interplay of the impulse (as determined by the added mass) and drag:

$$\frac{\mathrm{d}}{\mathrm{d}t}\left[\frac{2}{3}\pi\rho R_{eq}^3(t)\, C(t) U(t)\right] = -F_d(t), \tag{2.7}$$

where R_{eq} is the radius of a sphere having the same volume V as the bubble, $\frac{4}{3}\pi R_{eq}^3 = V$, C is the added mass coefficient for motion parallel to the symmetry axis, dependent on the bubble shape and equal to 1 for a sphere, and F_d is the drag force. An important effect of the translatory motion is the flattening of the bubble in the plane normal to its velocity, which tends to increase C (see e.g. § 7).

Upon rearranging (2.7), we find

$$\frac{\mathrm{d}U}{\mathrm{d}t} = -U\left(3\frac{\dot{R}_{eq}}{R_{eq}} + \frac{\dot{C}}{C}\right) - \frac{3}{2\pi C\rho R_{eq}^3}F_d. \tag{2.8}$$

This equation shows that a decrease of the bubble volume or of the added mass coefficient tends to increase the velocity of translation. Growth tends to stabilize the spherical shape (see e.g. Plesset & Prosperetti 1977; Prosperetti & Hao 1999) so that $\dot{C} \simeq 0$, $\dot{R}_{eq} > 0$, and a bubble rising in a superheated liquid will slow down. Conversely, a collapsing bubble flattens in the direction of motion, which gives $\dot{C} > 0$, even though $\dot{R}_{eq} < 0$. There is therefore the possibility of a near cancellation of these effects which, in the presence of gravity, would produce a nearly constant rise velocity as observed in some experiments (see Wittke & Chao 1967; Chen & Mayinger 1992; Legendre *et al.* 1998). In extreme cases, the positivity of $\dot{C}$ can more than compensate the effect of the volume reduction and the bubble can actually slow down even while collapsing, as found in the example shown in figure 8(*a*). In both cases, the radial velocity – and, therefore, the heat transfer at the bubble surface – plays a dominant role.

These considerations show that, as a consequence of translation, several competing effects appear. If the bubble collapses, its shrinking volume tends to increase the

https://doi.org/10.1017/S0022112008000670 Published online by Cambridge University Press

velocity thus accelerating heat removal, which is also aided by the shape deformation. This same deformation, on the other hand, increases the drag and the added mass, thus tending to limit the rate of increase of the velocity. Ultimately, the behaviour of the bubble depends on the balance of these competing effects.

3. Mathematical formulation

We append the subscript v to vapour quantities and the subscript s to quantities evaluated at the bubble surface; liquid quantities carry no subscript.

The liquid velocity and pressure fields, $\boldsymbol{u}$ and p, are governed by the incompressible Navier–Stokes equations and the liquid temperature T by the convection–diffusion equation

$$\frac{\partial T}{\partial t} + \boldsymbol{u}\cdot\nabla T = \alpha\nabla^2 T. \tag{3.1}$$

With the small temperature variations of present concern, all the physical properties of the liquid – density ρ, kinematic viscosity ν, thermal diffusivity α and thermal conductivity k – can be considered constant.

Slight temperature non-uniformities on the bubble surface would be rapidly annihilated by local evaporation and condensation over time scales much shorter than those characterizing the other phenomena of interest. Furthermore, in view of the very small inertia of the vapour, pressure gradients inside the bubble cannot persist beyond acoustic time scales of the order of microseconds. Thus, we model the bubble as a region of negligible mass with spatially uniform pressure. Since the rate of phase change is moderate and the vapour velocity is small with respect to the speed of sound, we assume thermodynamic equilibrium at the bubble surface (see e.g. Labuntsov & Kryukov 1979) and take p_v as the saturation pressure at the surface temperature T_s. These two quantities are related by the Clausius–Clapeyron relation,

$$\frac{\mathrm{d}p_v}{\mathrm{d}T_s} = \frac{L\rho_v}{T_s}, \tag{3.2}$$

with L the latent heat and ρ_v the vapour density, also spatially uniform. Over a limited temperature range, with the perfect-gas law for the vapour, this equation can be integrated keeping L constant to find

$$p_v = P_0 \exp\left(-\frac{L}{RT_s}\right) \tag{3.3}$$

with $P_0 = p_{v0}\exp(L/RT_{s0})$ a constant and R the universal gas constant divided by the vapour molecular mass.

Conservation of energy at the bubble surface requires that

$$(\boldsymbol{q} - \boldsymbol{q}_v)\cdot\boldsymbol{n} = L\rho_v(\boldsymbol{u}_v - \boldsymbol{v})\cdot\boldsymbol{n} \equiv L\dot{m}, \tag{3.4}$$

where $\boldsymbol{q} = -k\boldsymbol{n}\cdot\nabla T$ is the heat flux, $\boldsymbol{n}$ the unit normal directed out of the bubble, $\boldsymbol{u}_v$ the vapour velocity at the bubble surface, $\boldsymbol{v}$ the velocity of the interface, and $\dot{m}$ the local mass flux, which is positive for condensation. Upon integrating over the bubble surface $S(t)$ and neglecting spatial variations of ρ_v we find

$$L\frac{\mathrm{d}}{\mathrm{d}t}(\rho_v V) = \oint_{S(t)} (\boldsymbol{q}_v - \boldsymbol{q})\cdot\boldsymbol{n}\,\mathrm{d}S, \tag{3.5}$$

https://doi.org/10.1017/S0022112008000670 Published online by Cambridge University Press

where V is the bubble volume. The vapour-side heat flux $\boldsymbol{q}_v$ can be estimated as shown in Appendix A to find

$$L\frac{\mathrm{d}}{\mathrm{d}t}(\rho_v V) + \rho_v V c_s \frac{\mathrm{d}T_s}{\mathrm{d}t} = \oint_{S(t)} k(\nabla T \cdot \boldsymbol{n})\,\mathrm{d}S, \tag{3.6}$$

where $c_s = c_{pv} - L/T_s$ is the specific heat of the vapour along the saturation line, with c_{pv} the (constant) specific heat at constant pressure. The first term in the left-hand side of (3.6) represents the latent heat for the phase change, the second term represents the change of the vapour enthalpy and the right-hand side is the heat flux at the bubble surface from the liquid phase.

Conservation of mass at the interface requires that

$$\dot{m} = \rho_v(\boldsymbol{u}_v - \boldsymbol{v})\cdot\boldsymbol{n} = \rho(\boldsymbol{u} - \boldsymbol{v})\cdot\boldsymbol{n} \tag{3.7}$$

from which

$$\boldsymbol{u}\cdot\boldsymbol{n} = \boldsymbol{v}\cdot\boldsymbol{n} + \frac{\rho_v}{\rho}(\boldsymbol{u}_v - \boldsymbol{v})\cdot\boldsymbol{n} \simeq \boldsymbol{v}\cdot\boldsymbol{n} \tag{3.8}$$

in view of the smallness of ρ_v/ρ. Upon using this approximation, the equation of state, and the Clausius-Clapeyron relation, (3.6) becomes

$$\left(c_p + \frac{L^2}{RT_s^2} - \frac{2L}{T_s}\right)\frac{\mathrm{d}T_s}{\mathrm{d}t} = \frac{1}{\rho_v V}\oint_{S(t)} [k(\nabla T\cdot\boldsymbol{n}) - \rho_v L\boldsymbol{u}\cdot\boldsymbol{n}]\,\mathrm{d}S. \tag{3.9}$$

Since vapour inertia is neglected, the liquid tangential stress vanishes at the bubble surface, while the difference in the normal stresses is balanced by surface tension:

$$p_v = p - \boldsymbol{n}\cdot\boldsymbol{\tau}\cdot\boldsymbol{n} + \sigma\mathscr{C}, \tag{3.10}$$

in which $\boldsymbol{\tau}$ is the viscous stress in the liquid, σ the surface tension coefficient, also assumed constant, and $\mathscr{C}$ the local curvature.

4. Numerical formulation

The computations were carried out on an orthogonal boundary-fitted grid (ξ, η) generated in the meridian plane by the technique of Duraiswami & Prosperetti (1992), which belongs to the family of orthogonal mappings proposed by Ryskin & Leal (1983) and already used e.g. in Takagi, Matsumoto & Huang (1997), Yang, Prosperetti & Takagi (2003) and Yang & Prosperetti (2006). The computational domain, shown in figure 1, is bounded by the bubble surface, the symmetry axis and an outer boundary given as a sphere of radius $20R_{eq}$ centred at the midpoint between the front and rear stagnation points on the bubble surface on the symmetry axis. A new grid is generated after each update of the bubble position and shape. Thus, although the grid is always centred on the bubble, the calculation is effectively conducted in the laboratory frame as was done in our earlier paper (Yang & Prosperetti 2006).

Figure 1 shows an example of the overall numerical grid and a detail of the grid near the bubble surface. The coordinate ξ varies in the direction parallel to the bubble surface, while η is normal to it. The bubble surface corresponds to $\eta = 1$, the outer boundary to $\eta = 0$, the part of the symmetry axis ahead of the bubble to $\xi = 0$ and the part downstream to $\xi = 1$.

The form of the continuity and momentum equations in these coordinates is standard and is the same used in several earlier papers (e.g. Takagi *et al.* 1997; Yang

https://doi.org/10.1017/S0022112008000670 Published online by Cambridge University Press

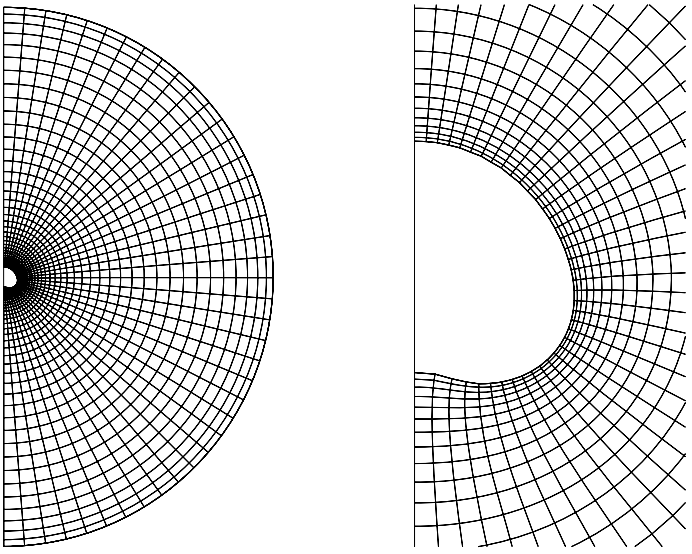


FIGURE 1. Example of the computational domain and boundary fitted grid.

et al. 2003; Yang & Prosperetti 2006). The liquid energy equation in orthogonal coordinates (ξ, η) is

$$\frac{\partial T}{\partial t} + \left(\frac{u_\xi}{h_\xi}\frac{\partial T}{\partial \xi} + \frac{u_\eta}{h_\eta}\frac{\partial T}{\partial \eta}\right) = \frac{\alpha}{h_\xi h_\eta r}\left[\frac{\partial}{\partial \xi}\left(\frac{h_\eta r}{h_\xi}\frac{\partial T}{\partial \xi}\right) + \frac{\partial}{\partial \eta}\left(\frac{h_\xi r}{h_\eta}\frac{\partial T}{\partial \eta}\right)\right] + \frac{1}{h_\xi h_\eta}\left[\left(\frac{\partial r}{\partial \eta}\frac{\partial T}{\partial \xi} - \frac{\partial r}{\partial \xi}\frac{\partial T}{\partial \eta}\right)\frac{\partial x}{\partial t} + \left(\frac{\partial x}{\partial \xi}\frac{\partial T}{\partial \eta} - \frac{\partial x}{\partial \eta}\frac{\partial T}{\partial \xi}\right)\frac{\partial r}{\partial t}\right], \quad (4.1)$$

where u_ξ, u_η are the liquid velocity components, h_ξ and h_η the scale factors, and r the distance from the symmetry axis.

The free surface is updated by integrating

$$\frac{\mathrm{d}\boldsymbol{x}_s}{\mathrm{d}t} = \boldsymbol{u}(\boldsymbol{x}_s, t), \quad (4.2)$$

i.e. essentially (3.8). Since the grid follows the bubble shape, it has a velocity which needs to be properly accounted for in the evaluation of the convective terms for both momentum and temperature (see e.g. Yuan & Prosperetti 1997).

The explicit form of the tangential and normal stress conditions at the bubble surface $\eta = 1$ is given in e.g. Takagi *et al.* (1997) and Yang & Prosperetti (2006). On the symmetry axis $\xi = 0$ and $\xi = 1$ the natural conditions are

$$u_\xi = 0, \qquad \frac{\partial u_\eta}{\partial \xi} = 0. \quad (4.3)$$

The normal gradient of the tangential velocity is taken to vanish on the outer boundary $\eta = 0$ while the discretized form of the incompressibility condition $\nabla \cdot \boldsymbol{u} = 0$ is used to obtain the normal velocity. Furthermore, pressure and temperature are kept at the local undisturbed values.

4.1. *Algorithm*

The continuity, momentum and energy equation are discretized by second-order accurate finite differences on a staggered grid and solved by a pressure-increment

https://doi.org/10.1017/S0022112008000670 Published online by Cambridge University Press

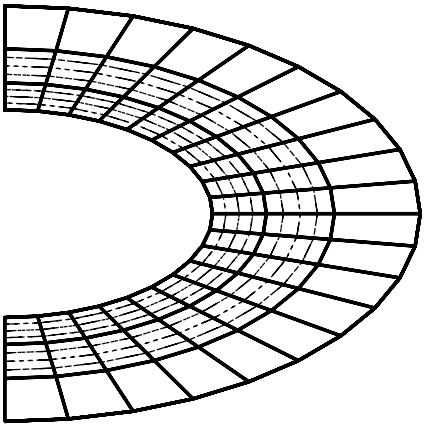


FIGURE 2. The grid for the energy equation is a refinement of the boundary fitted grid of the previous figure obtained by interpolation in the normal direction.

projection method with semi-implicit discretization for the nonlinear terms (see Brown, Cortez & Minion 2001); the method is a slight modification of that described in detail in Yang & Prosperetti (2006). The standard Neumann conditions for the auxiliary pressure variable are imposed on all the boundaries. The method has second-order accuracy in space and time. The sequence of the calculation is as follows:

1. The free-surface position is advanced to the next time level t^{n+1} with a third-order Adams–Bashforth method using (4.2).
2. A new outer boundary is constructed as described before.
3. An orthogonal boundary-fitted grid is generated.
4. The field equations are solved by the iterative procedure described in Yang & Prosperetti (2006) extended to include the energy equation, which is solved with the Dirichlet condition $T = T_s$ at the bubble surface. To calculate $T_s(t^{n+1})$ use is made of (3.9) in which the integral on the right-hand side is evaluated at the previous iteration. The knowledge of T_s also specifies the vapour pressure, which is needed as a boundary condition for the solution of pressure Poisson equation.

The grid was generated with the distortion function (Duraiswami & Prosperetti 1992)

$$f = M\frac{a}{b-\eta^2} \tag{4.4}$$

with M the conformal modulus and a and b parameters, only one of which is free (see Duraiswami & Prosperetti 1992). Several values of a and b were tested for each case.

In the situations of present concern, the thermal boundary layer is thinner than the momentum boundary layer. In order to resolve the former without unnecessarily refining the entire grid, for the energy equation we used a finer grid near the bubble surface. This finer grid was generated by linear interpolation in the direction normal to the bubble surface from the original momentum grid as shown in figure 2 where four cells are constructed in each momentum cell. The velocity field on the finer grid is linearly interpolated from the momentum grid. The relatively large aspect ratio of the thermal cells does not cause problems because the temperature gradients parallel to the bubble surface are small as the surface temperature is uniform. Since the need for high resolution only exists near the bubble surface, the finer grid was only constructed out to a maximum radius of $4.4R_{eq}(t)$, which was found to give satisfactory results. The interpolation procedure does not guarantee solenoidality of

https://doi.org/10.1017/S0022112008000670 Published online by Cambridge University Press

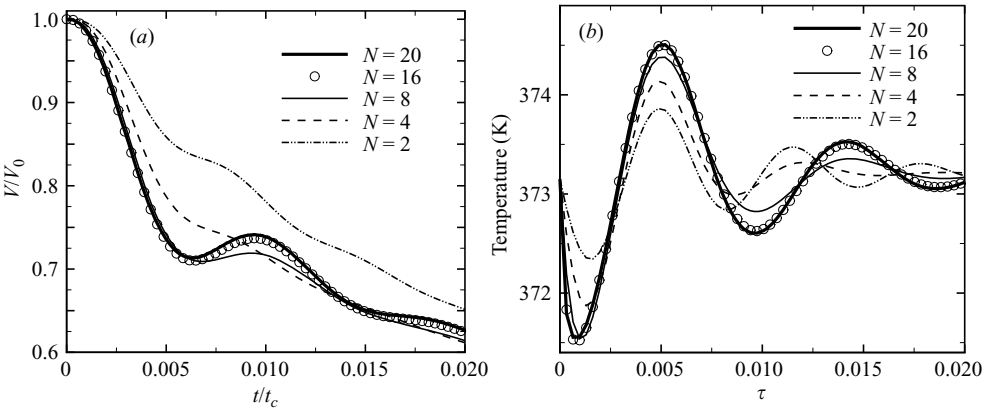


FIGURE 3. Test of the thermal grid resolution for the collapse of a 1 mm-radius spherical bubble at rest in water at a constant ambient pressure of 101.3 kPa with a liquid subcooling of 3.35 K ($Ja = 10$): (*a*) volume; (*b*) surface temperature. Here N is the number of new cells for the thermal calculation in each original cell of the fluid dynamics calculation, $\tau = t/t_c$, and $t_c = 46.2$ ms, as defined in (2.2).

the interpolated velocity field. While this would be a serious concern for the solution of the momentum equation, it is a very minor one for the convection–diffusion equation.

5. Validation

The code used in the present work was built on an earlier one without heat transfer or phase change which was extensively validated as described in Yang & Prosperetti (2006). To test the accuracy of the present code, we simulated the collapse of a spherical vapour bubble at rest. A spherically symmetric model for this situation was presented in Hao & Prosperetti (1999) and Hao & Prosperetti (2000), and the results of that model were used for validation.

Figure 3 gives an example of the grid dependence of the thermal calculation. This figure shows the effect of different levels of refinement of the momentum grid on the bubble volume and surface temperature. It is seen that, in this case for which the momentum grid used 41×41 nodes, convergence is obtained with about $N = 16$ thermal cells in each momentum cell. With $N = 16$, the smallest grid spacing, achieved in the first cell adjacent to the bubble surface, is $\delta/R(0) = 0.001\,08$ for the initial grid. Further tests showed that a smallest grid spacing of about $\delta/R(0) = 0.001$ ensured a grid-independent solution for all the cases described in this paper.

A comparison with the results of the spherical model is shown in figure 4, where the circles representing the present results are seen to agree well with the spherical model predictions (solid lines). The two sets of results compare well throughout the collapse process. The early stages, where the non-monotonic collapse is due to the competing effects of inertia and phase change (see Hao & Prosperetti 1999), provide an especially stringent test of the accuracy of the phase change and heat transport calculation.

In these simulations, as well as those that follow, the physical properties of saturated water at 101.3 kPa pressure and 373.15 K temperature were used: $\rho = 955.1\,\mathrm{kg\,m^{-3}}$, $\nu = 0.279\,55 \times 10^{-6}\,\mathrm{m^2\,s^{-1}}$, $k = 0.684\,\mathrm{W\,m^{-1}\,K^{-1}}$, $\alpha = 0.169\,87 \times 10^{-6}\,\mathrm{m^2\,s^{-1}}$, $L = 2.2572\,\mathrm{MJ\,kg^{-1}}$, and $\sigma = 0.059\,\mathrm{N\,m^{-1}}$. All calculations were started with an

https://doi.org/10.1017/S0022112008000670 Published online by Cambridge University Press

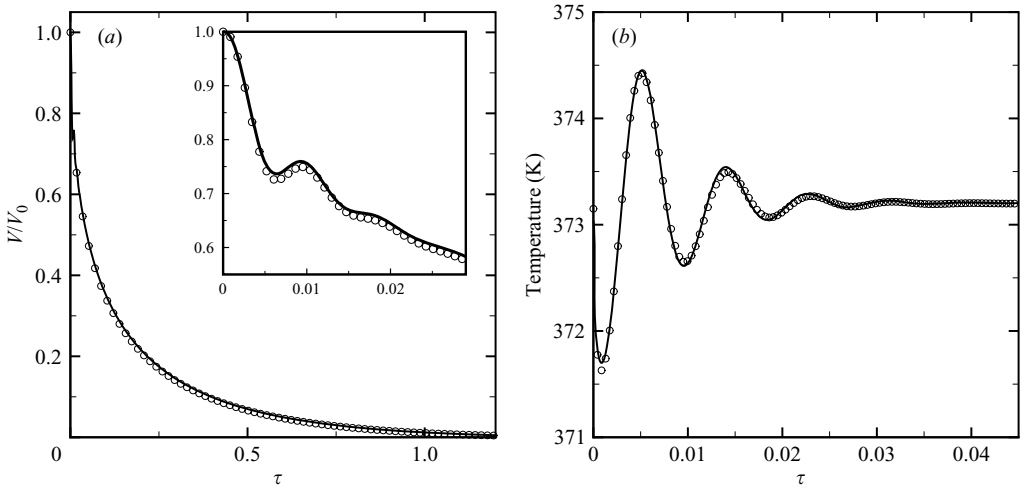


FIGURE 4. Comparison of the present results (circles) with those of the spherical model for the collapse of a stationary 1 mm radius spherical bubble in water at 101.3 kPa ambient pressure with a subcooling of 3.35 K ($Ja = 10$): (*a*) volume; (*b*) surface temperature. Here $\tau = t/t_c$, with $t_c = 46.2$ ms, as defined in (2.2); grid refinement $N = 16$,

initially spherical bubble, with a vapour temperature $T_s(0) = 373.15$ K, and $p_v(0) = P_\infty = 101.33$ kPa.

In most of the experiments reported in the literature, the bubbles form at a nucleation site on a solid wall, detach and rise by buoyancy (see e.g. Abdelmessih, Hooper & Nangia 1972; Moalem & Sideman 1973; Chen & Mayinger 1992; Kalman & Ullmann 1999). In these conditions, the bubbles undergo at the same time strong shape oscillations and accelerating motion, neither of which is included in the present model. The experimental conditions that most approach those of the present calculations are those of Wittke & Chao (1967), even though the liquid they used was not thoroughly degassed. The build-up of an incondensible gas layer at the vapour–liquid interface is known to slow down the condensation rate (see e.g. Prosperetti & Hao 2002) and, furthermore, the bubble does not disappear completely.

Figure 5 shows a comparison of Wittke & Chao (1967)'s data for their figure 5 (circles) with our simulation of the same case (solid line) and their theoretical model (diamonds). The bubble had an initial radius of 3.93 mm and an initial velocity of 22 mm s^{-1}; the water subcooling was 5.49 K, the Jacob number 16.7 and the initial Péclet number 1029. We chose this case as it corresponds to the most degassed conditions among those reported in the paper and we focus here on approximately the first half of the condensation process, which presumably is less affected by the presence of the residual incondensible gas. Our results are significantly closer to the data than Wittke & Chao's own theory.

6. Translating bubble in an isothermal liquid

In this section we study the collapse of a condensing bubble translating in an initially isothermal liquid. This problem has been studied by several investigators under the assumption that the bubble maintains a spherical shape (see e.g. Gumerov 1996; Legendre *et al.* 1998; Hao & Prosperetti 2000); recently, the spherical

https://doi.org/10.1017/S0022112008000670 Published online by Cambridge University Press

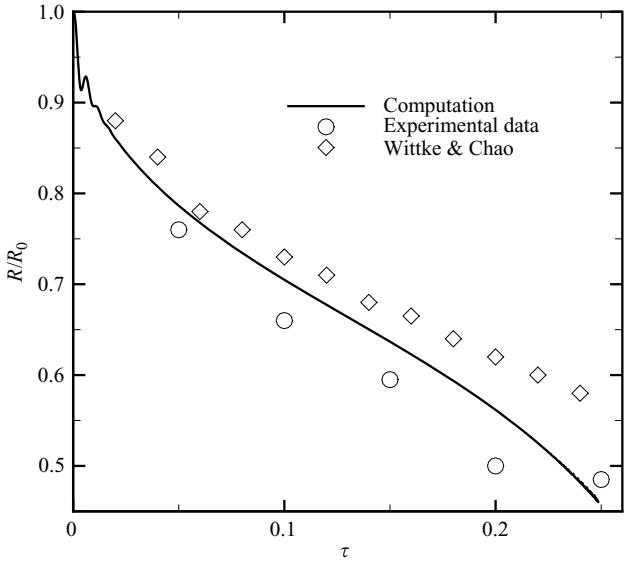


FIGURE 5. Comparison of the present result (solid line) with the data of figure 5 of Wittke & Chao (1967) for $Ja = 16.7$, $Pe = 1029$; the diamonds are Wittke & Chao's theoretical prediction. Here $\tau = t/t_c$, with $t_c = 259$ ms.

approximation has been applied by Ivashnyov & Smirnov (2004) to the growth process.

The bubble is taken to be initially spherical and the liquid velocity is initialized with the potential flow solution. The initial temperature field is uniform and equal to T_∞. A grid with 41×41 nodes was used in the calculations.

As a representative case we consider $R(0) = 1$ mm, a 5 K liquid subcooling and an initial velocity is $0.127\,\mathrm{m\,s^{-1}}$. These conditions correspond to $Ja = 14.9$, $t_c = 20.7$ ms, $Pe = 1495$ and $We = 0.261$. Figure 6 shows the time evolution of the bubble volume. Here the solid line is the spherical model of Hao & Prosperetti (2000) and the dashed line the simplified model of § 7. A comparison of the various results will be found in the next section.

The initial sudden exposure of the vapour to the subcooled liquid causes a rapid condensation and a fast collapse which, by inertia, compresses the vapour and causes a temporary rebound followed by a barely visible second one. During this initial phase the bubble surface temperature deviates markedly from the saturation value at the ambient pressure. Experimentally, the situation simulated here could be realized with a step increase in the system pressure. In subcooled boiling a more typical case would be a bubble detaching from the heated wall and being transported to a cooler liquid region. The difficulty in modelling such a situation as an initial condition in a simulation of the present type is discussed in Hao & Prosperetti (2000). After the initial transient, the collapse is monotonic and the surface temperature essentially remains constant at saturation.

Figure 7 illustrates the bubble shape at different instants and figure 8(*a*) shows the translational velocity, defined as in Yang *et al.* (2003). The vorticity distribution in the bubble wake (not shown here) is very similar to that prevailing in steady flow (see e.g. Yang & Prosperetti 2007). In particular, no vorticity is shed in this or any of the

https://doi.org/10.1017/S0022112008000670 Published online by Cambridge University Press

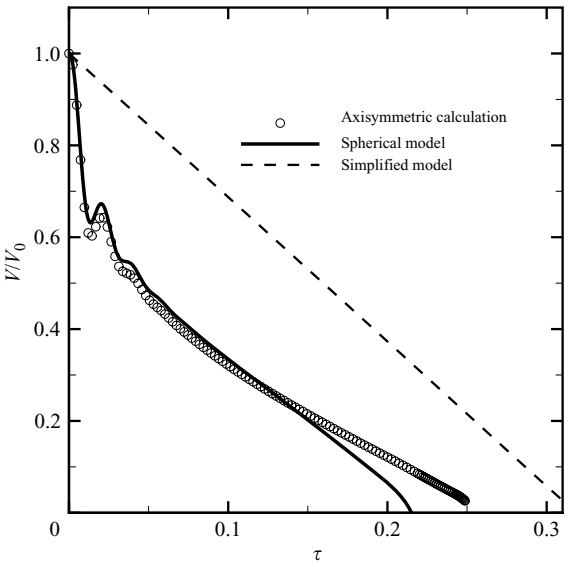


FIGURE 6. Volume versus time for the collapse of an initially spherical bubble with a radius of 1 mm translating with an initial velocity of $0.127\,\mathrm{m\,s^{-1}}$ in water at 101.3 kPa ambient pressure subcooled by 5 K ($Ja = 14.9$); here $\tau = t/t_c$ with $t_c = 20.7$ ms, as defined in (2.2). The circles are the results of the present model, the solid line the spherical model of Hao & Prosperetti (2000) and the dashed line the simplified model of § 7.

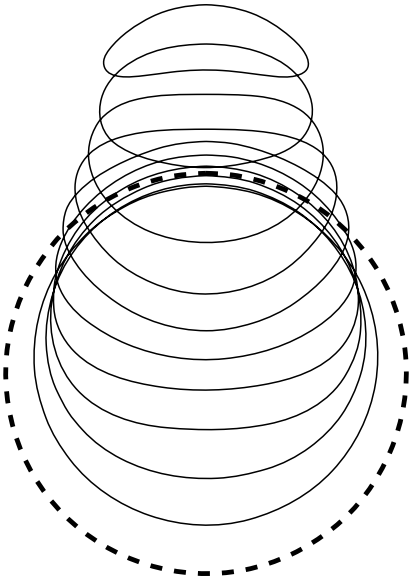


FIGURE 7. Bubble shapes for the same case of figure 6. Time interval between each shape is $0.025t_c$, which equals 0.5 ms, with the initial shape represented by the dashed line.

other cases that we have studied. There is also a long period (from about $t/t_c = 0.04$ to $t/t_c = 0.14$) of nearly constant velocity, a possibility mentioned in § 2.

It is remarkable that the increase of surface tension effects with decreasing volume appears to be insufficient to stabilize the spherical shape so that there

https://doi.org/10.1017/S0022112008000670 Published online by Cambridge University Press

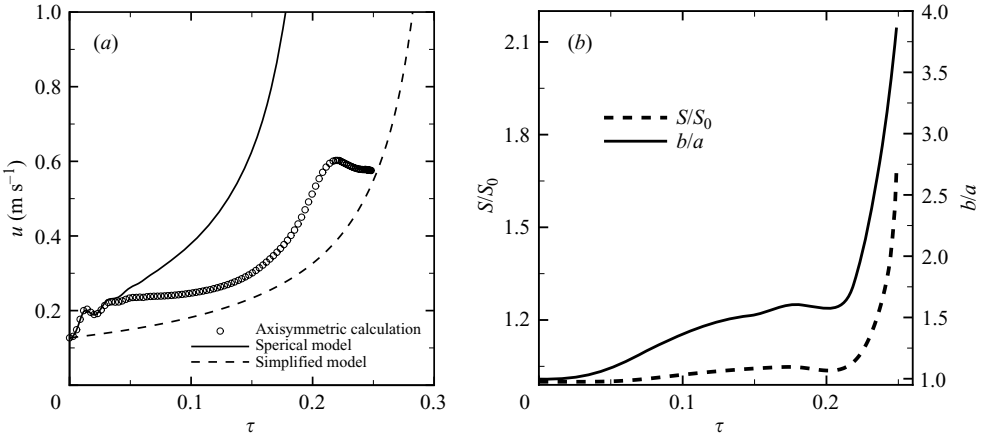


FIGURE 8. (*a*) Bubble velocity versus time for the vapour bubble collapse of figures 6 and 7. The circles are the results of the present model, the solid line the spherical model of Hao & Prosperetti (2000) and the dashed line the simplified model of § 7. (*b*) Evolution of the bubble surface area S/S_0 normalized by the area of a sphere with the same volume (dashed line, left axis) and aspect ratio b/a (solid line, right axis) for the same case; a is defined as the distance between the stagnation points on the symmetry axis, and $b/2$ as the maximum distance of the bubble surface from the symmetry axis.

are strong deviations from sphericity, accompanied by shape oscillations. For the last shape shown the bubble velocity is about $U = 0.576\,\mathrm{m\,s^{-1}}$ and its equivalent radius $R_{eq} = 0.295\,\mathrm{mm}$. The instantaneous Weber number is $2R_{eq}\rho U^2/\sigma = 3.33$, large enough for pressure forces to overpower the stabilizing effect of surface tension. This would not have happened had the initial velocity not been amplified by the tendency to preserve the initial impulse. The distortion near the end of the collapse has a strong effect on the velocity as shown in figure 8(*a*): the large increase in the added mass coefficient causes a velocity decrease in spite of the diminishing volume.

Figure 8(*b*) shows the surface area, normalized by that of a sphere with an equal volume (dashed line), and the aspect ratio, defined as the ratio of the maximum diameter to the distance between the two stagnation points (solid line); for a sphere, of course, both quantities equal 1. The slight oscillations of the aspect ratio correspond to the shape oscillations visible in figure 7.

Figure 9 shows the temperature contours during the collapse process. The eight isotherms shown in each figure are spaced by 0.66 K between 372.41 K and 368.444. The thermal boundary layer is thinner around the front surface and thicker at the rear. At the rear of the bubble, the isotherms curve forward slightly as, having passed closer to the bubble surface than that farther away, the liquid here is slightly warmer.

The instantaneous streamlines at $t/t_c = 0.1$ and $t/t_c = 0.2$ are shown in figure 10 in the rest frame of the bubble. At the rear of the bubble, the velocity of the incoming flow is opposite that caused by the collapse, which produces a stagnation point on the axis of the wake. Note that this phenomenon is quite different from the attached wake found in the work of Ryskin & Leal (1984), Leal (1989) and Blanco & Magnaudet (1995), which only begins to exist for an aspect ratio of about 1.7, larger than that exhibited by the bubble at these instants.

As another example, we consider a subcooling of 3.35 K and the same initial velocity. In this case, $Ja = 10$, $t_c = 46.2\,\mathrm{ms}$, $Pe = 1495$ and $We = 0.261$. The results are shown in figure 11 and do not differ qualitatively from the previous ones, except for

https://doi.org/10.1017/S0022112008000670 Published online by Cambridge University Press

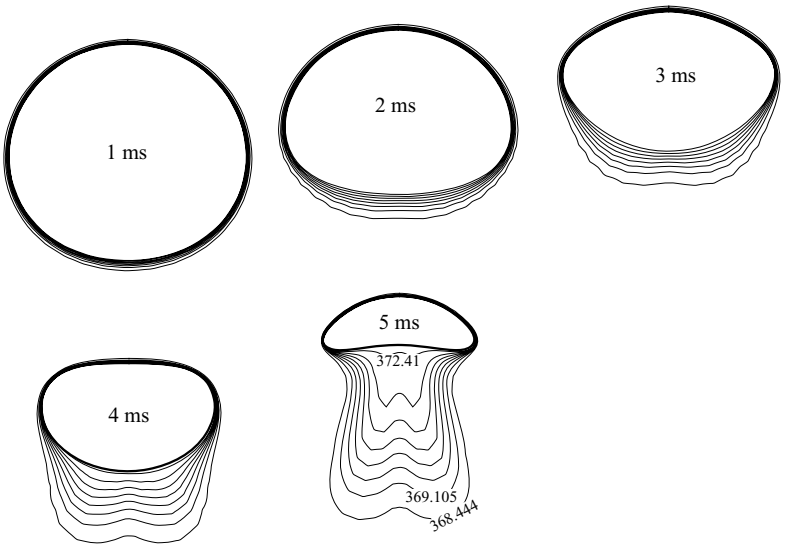


FIGURE 9. Isotherms for the vapour bubble collapse case of figure 6; eight isotherms spaced by 0.66 K are shown in each frame. The isotherm closest to the bubble has a temperature of 372.41 K, the one farthest away 368.444. The time interval between successive frames is $0.05t_c = 1$ ms.

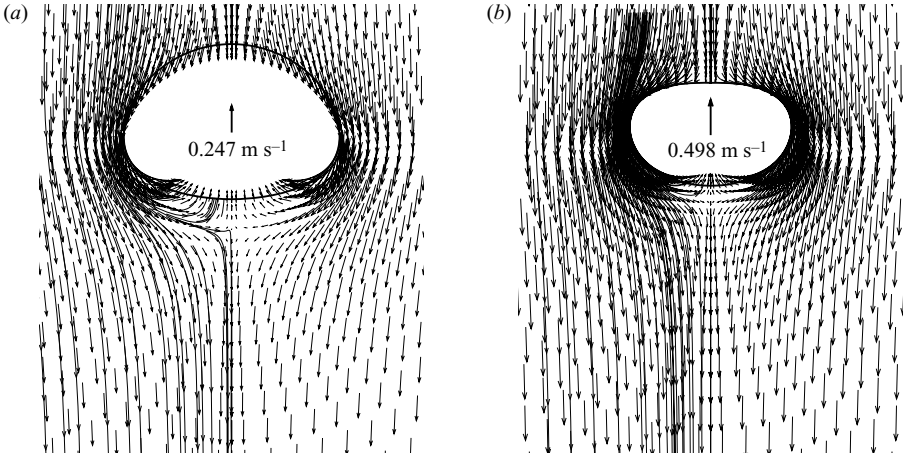


FIGURE 10. Instantaneous streamlines and velocity fields at (*a*) $t/t_c = 0.1$ and (*b*) $t/t_c = 0.2$ for the case of figure 6.

the fact that the collapse is less violent and therefore the velocity of translation grows less. For the last shape shown here (somewhat earlier in the collapse history than that of figure 7), $R_{eq} = 0.625$ mm, $U = 0.366$ m s^{-1} with a corresponding Weber number 2.84. Although not much smaller than in the previous example, this value indicates that surface tension has a relatively greater importance and the bubble deforms less.

7. Discussion

Hao & Prosperetti (2000) presented a theory for the condensation of a translating vapour bubble in which the bubble velocity was calculated by a simple model

https://doi.org/10.1017/S0022112008000670 Published online by Cambridge University Press

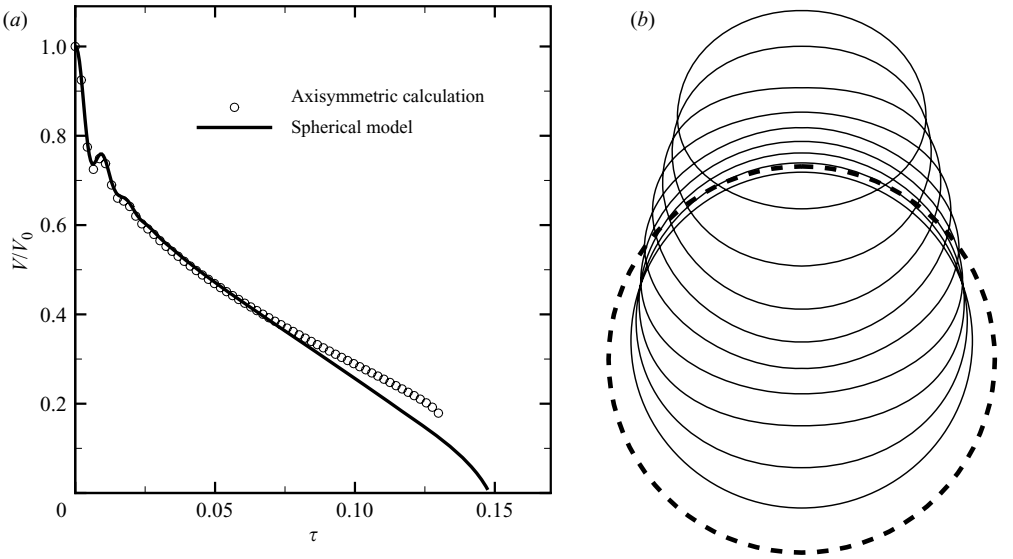


FIGURE 11. (*a*) Volume versus time for the collapse of an initially spherical bubble with a radius of 1 mm translating with an initial velocity of $0.127\,\mathrm{m\,s^{-1}}$ in water at 101.3 kPa ambient pressure subcooled by 3.35 K ($Ja = 10$); here $\tau = t/t_c$ with $t_c = 46.2$ ms, as defined in (2.2). The circles are the results of the present model and the solid line the spherical model of Hao & Prosperetti (2000). (*b*) Successive shapes of the bubble at time intervals of $0.0135t_c = 0.625$ ms; the initial shape is represented by the dashed line.

balancing added mass and drag for a sphere as in (2.7) with $C = 1$, and the convection–diffusion energy equation around the bubble was solved by approximating the flow field as potential. The results of this model are shown by the solid lines in figures 6, 8(*a*) and 11(*a*).

The general first impression that the two calculations give close results for the bubble volume versus time (figure 6) needs to be qualified. It must be kept in mind that the quantity shown is the volume, rather than the radius. When the volume has decreased by a factor of 5, the radius has decreased only to 58 % of the initial value. A graph of $R_{eq}/R(0)$ would therefore reveal far larger differences. On the other hand, the energy content of the bubble is proportional to the volume, so that the condensation time is strongly dominated by the initial part of the process. In this sense, for some practical purposes, the two models may be thought of as giving reasonably close results.

A consideration of the relation of the solid lines in figures 8(*a*) and 11(*a*) (spherical model) with the circles (present model) reveals significant differences. Figure 8(*a*) shows that the translational velocity of the present model is significantly smaller than that of the spherical model. As (2.7) suggests, this difference must be due at least in part to a different condensation rate. Indeed, the slope of the $V(t)$ line for the spherical model in figures 6 and 11(*a*), proportional to the total condensation rate, is larger than the present one.

The heat flux at the bubble surface differs not only quantitatively, but also qualitatively between the two models as shown in figure 12. Here, the temperature gradient at the bubble surface $\boldsymbol{n}\cdot\nabla T(\theta)$, normalized by its value at the front stagnation point $\boldsymbol{n}\cdot\nabla T(0)$, is plotted as a function of the polar angle measured from the front

https://doi.org/10.1017/S0022112008000670 Published online by Cambridge University Press

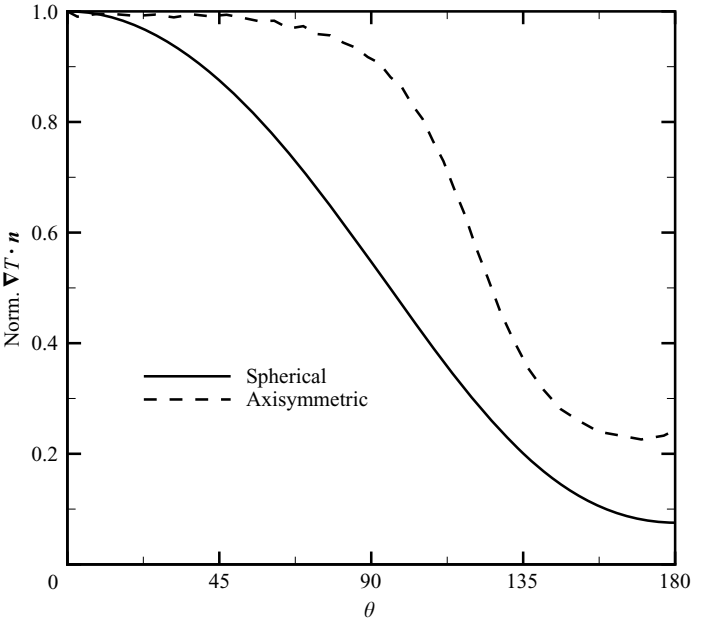


FIGURE 12. Temperature gradient at the bubble surface normalized by its value at the front stagnation point as a function of the polar angle measured from the front stagnation point at $t/t_c = 0.1$ for the case of figure 6. The solid line is the spherical model and the dashed line the present model.

stagnation point at $t/t_c = 0.1$ for the case of figure 6. At the instant shown, the translational velocities for the two models are already rather different (figure 8*a*); the absolute values of the gradients at the stagnation point are 198 K mm^{-1} for the present model and 284 K mm^{-1} for the spherical model. A striking feature of the result is the strongly different spatial distribution of the temperature gradient which is nearly constant over the front half of the bubble for the present model. This feature appears to be a consequence of the flattening of the bubble shape. The radius of curvature on the axis of symmetry for a spheroid of aspect ratio χ is a factor $\chi^{4/3}$ larger than the equivalent spherical radius which, for $\chi \simeq 1.5$ (see figure 8*b*), is about 1.72. For a given incident velocity, a flatter shape gives rise to a more strongly accelerating flow away from the stagnation point which thins the thermal boundary layer and increases the heat transfer. This enhancement of the heat transfer offsets to some extent the effect of the smaller translational velocity with the consequence that $\mathrm{d}V/\mathrm{d}t$ is different in the two models (figure 6) but not as much as the difference between the velocities (figure 8*a*) would suggest. It is also interesting to point out that, since the vapour condensation rate is proportional to the liquid temperature gradient at the bubble surface, the lines in figure 12 also represent the distribution of the condensation flux over the bubble surface.

According to the theory of Levich (1962) and Ruckenstein (1959), the quantity shown in figure 12 should equal

$$\frac{\boldsymbol{n}\cdot\nabla T(\theta)}{\boldsymbol{n}\cdot\nabla T(0)} = \sqrt{3}\,\frac{\cos^2\tfrac{1}{2}\theta}{\sqrt{2+\cos\theta}} \tag{7.1}$$

https://doi.org/10.1017/S0022112008000670 Published online by Cambridge University Press

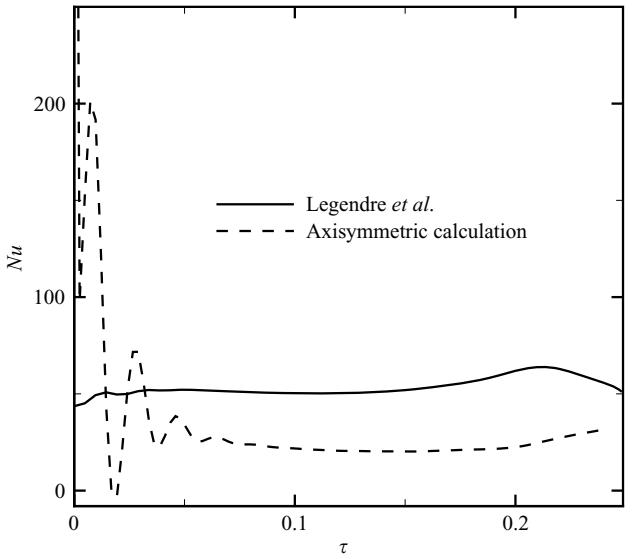


FIGURE 13. Time evolution of the Nusselt number based on the average heat transfer coefficient (7.3) and equivalent spherical radius for the vapour bubble collapse of figure 6 (dashed line) compared with the relation (2.6) (solid line).

with

$$\boldsymbol{n}\cdot\nabla T(0) = \frac{T_{sat} - T_\infty}{R}\sqrt{\frac{3}{\pi}Pe}. \tag{7.2}$$

The relation (7.1) is fairly close to the spherical model of Hao & Prosperetti (2000) (solid line in figure 12), which is perhaps not too surprising in view of the fact that both results are based on the potential velocity distribution around a sphere. The difference between the theory underlying (7.1) and the spherical model is the use, in the former, of a thin boundary layer assumption and a quasi-static approximation.

With the bubble radius and velocity calculated from the spherical model at $t/t_c = 0.1$, $R = 0.694$ mm, $U = 0.380\,\mathrm{m\,s^{-1}}$, (7.2) gives $392\,\mathrm{K\,mm^{-1}}$ while, as already noted, the spherical model gives $284\,\mathrm{K\,mm^{-1}}$. A major component of this difference is probably the neglect of the bubble wall motion underlying (7.2). For the case of a growing bubble, the analysis of Ruckenstein & Davis (1971) shows a strong dependence of the boundary layer thickness on $(\mathrm{d}R/\mathrm{d}t)/U$, and this dependence may be expected to be even stronger for collapse, for which the geometrical thinning associated with growth turns into a thickening, with a corresponding decrease of the heat flux. At the instant under consideration, $-\mathrm{d}R/\mathrm{d}t = 0.089\,\mathrm{m\,s^{-1}}$, which is about 23 % of the translational velocity. As for the assumption of a thin thermal boundary layer, the results of Legendre *et al.* (1998) imply that, for $Ja = 10$ as here, its validity is quite restricted to the very early stages of the process. Figure 9 also illustrates the limitations of assuming a thin thermal layer all around the bubble.

It is interesting to compare the Nusselt number calculated from the numerical results with the estimate (2.6) of Legendre *et al.* (1998). Such a comparison is provided in figure 13, in which the mean heat transfer coefficient was obtained from

$$h = -\frac{1}{4\pi R_{eq}^2(T_{sat} - T_\infty)}\oint_S \boldsymbol{n}\cdot\nabla T\,\mathrm{d}S \tag{7.3}$$

https://doi.org/10.1017/S0022112008000670 Published online by Cambridge University Press

and the calculated value of the equivalent radius was used in the definition of Nu; the Péclet number was obtained from the calculated equivalent radius and instantaneous bubble velocity. The initial large oscillations are related to the mechanism causing a non-monotonic collapse mentioned before, which is not included in the physical picture leading to (2.6), represented by the solid line. Aside from this feature, there is fair agreement between the two results. The Levich–Ruckenstein approximation (2.4), on the other hand, is found to overestimate the Nusselt number by a factor of approximately 2. Since the area under the curve of the present model in figure 12 is larger than that under the latter model, it must be concluded that the overestimation of the Nusselt number is related to an overestimation of the temperature gradient at the front stagnation point as discussed before for $t/t_c = 0.1$.

It may be of some interest to develop further the relations presented in § 2. By approximating the bubble shape as an ellipsoid with semiaxes a and b, with $a < b$, and assuming a large Reynolds number, Moore (1965) calculated the aspect ratio $\chi = b/a$. When the Weber number, defined by,

$$We = \frac{2R_{eq}\rho U^2}{\sigma} \tag{7.4}$$

is 1 or less, his result may be approximated to within 3 % by

$$\chi \simeq 1 + \frac{9}{64}We. \tag{7.5}$$

Moore (1965) also calculated the effect of the deformation on the (steady) drag coefficient:

$$C_d = \frac{F_d}{\frac{1}{2}\pi\rho R_{eq}^2 U^2} = \frac{48}{Re}\,G(\chi), \tag{7.6}$$

where $Re = 2R_{eq}U/\nu$ is the Reynolds number defined in terms of the equivalent diameter and G is a function of the aspect ratio equal to 1 for $\chi = 1$.

The added mass coefficient of an oblate ellipsoid is well known (see e.g. Milne-Thomson 1960); it may be written as

$$C = 2\chi^2\,\frac{\sqrt{\chi^2-1} - \sec^{-1}\chi}{\chi^2\sec^{-1}\chi - \sqrt{\chi^2-1}}. \tag{7.7}$$

In the range of interest here, numerically, this function can be approximated very closely by

$$C \simeq (1+a)\chi - a \qquad a \simeq 0.275. \tag{7.8}$$

Upon substituting the previous relations into (2.8) we find

$$\left(1 + \frac{9}{32}\frac{1+a}{C}We\right)\frac{1}{U}\frac{\mathrm{d}U}{\mathrm{d}t} = -3\left(1 + \frac{3}{64}\frac{1+a}{C}We\right)\frac{1}{R_{eq}}\frac{\mathrm{d}R_{eq}}{\mathrm{d}t} - \frac{36U}{CR_{eq}}\frac{G(\chi)}{Re}. \tag{7.9}$$

To complete the model one needs an equation for the equivalent radius, for which we simply use

$$L\rho_v(T_{sat})\frac{\mathrm{d}}{\mathrm{d}t}\left(\frac{4}{3}\pi R_{eq}^3\right) = -4\pi R_{eq}^2 h(T_{sat} - T_\infty) \tag{7.10}$$

with the heat transfer coefficient given by (2.6). The temperature of the bubble surface is kept fixed at T_{sat} for the entire calculation.

https://doi.org/10.1017/S0022112008000670 Published online by Cambridge University Press

The results of this simplified model are shown by the dashed lines in figures 6 and 8(*a*). The most noticeable differences are due to the lack of the initial rapid condensation of the other two models which, as noted before, may correspond to a rather specific experimental situation. Even neglecting this aspect, however, significant differences are clearly seen, especially in the velocity result of figure 8(*a*), where the simplified model seems incapable of reproducing both the nearly constant velocity portion and the final slowdown of the present model.

8. Non-uniform temperature fields

We now consider two idealized models describing the behaviour of a bubble entering a subcooled or superheated liquid region. We consider both the case in which this region is 'thick' and that in which it is 'thin', in a sense which will be clear from the results presented. The boundary between the different temperature regions is idealized as a thin layer perpendicular to the direction of motion of the bubble. These calculations were carried out with a mesh having 61 nodes along the bubble surface and 41 nodes in the orthogonal direction.

8.1. *Thick subcooled liquid region*

As an example of the interaction with an extended subcooled liquid region, we consider a bubble with an initial radius of 1 mm and an initial velocity of $0.127\,\mathrm{m\,s^{-1}}$, initially set at the boundary between saturated water at 373.15 K and 101.3 kPa and water subcooled by 3.35 K. The conditions assumed for the subcooled liquid would correspond to $Ja = 10$, $t_c = 46.2$ ms, $Pe = 1495$ and $We = 0.261$.

The temperature field and the bubble shape for these conditions are shown at different instants in figure 14. In the first frame, near the boundary between the two liquid regions, there are clearly visible small wiggles caused by the fact that the boundary of the subcooled region is not aligned with the grid lines. Diffusion quickly smooths out these features over the first several time steps. We tested the consequences of this numerical artefact by comparing the computational results obtained with different grids, finding that an increase of the computational cells by 30 % led to only small differences in the instantaneous volume $V(t)$. This result could be expected as the uniformity of the bubble surface temperature effectively 'short-circuits' temperature differences in its neighbourhood. A similar test was conducted for all the cases described in this section. Thus, while we cannot claim complete grid independence in a strictly numerical sense, we believe that the results that we show are essentially converged.

Figures 14 and 15(*b*) clearly show the strong acceleration that the bubble undergoes as it starts condensing upon entering the subcooled region. The notion of drift is well established in fluid mechanics (see e.g. Darwin 1953; Lighthill 1956; Eames, Belcher & Hunt 1994; Sardić-Mitrović, Mohamed & Fernando 1999). It is also well known that when a bubble or particle traverses the interface between two liquids it carries some of the downstream fluid into the upstream one (see e.g. Hashimoto & Kawano 1990; Kawano, Hashimoto & Ihara 1996; Sardić-Mitrović *et al.* 1999). A similar effect is observed here, with some of the warmer liquid brought into the cold region.

The same problem was calculated using the spherical model of Hao & Prosperetti (2000). The numerical algorithm in the original paper was modified slightly to reflect the current initial temperature distribution; it was necessary to use 64 terms in the Legendre polynomial expansion and 32 terms in the Chebyshev polynomial expansion

https://doi.org/10.1017/S0022112008000670 Published online by Cambridge University Press

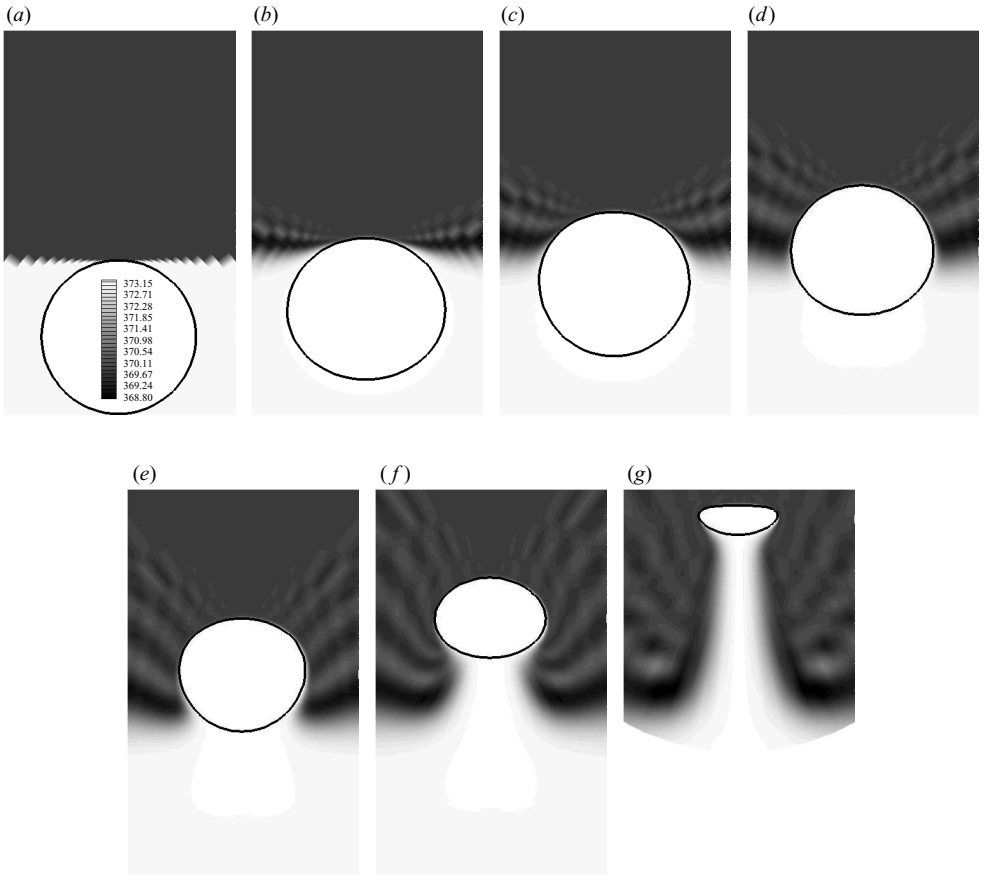


FIGURE 14. Instantaneous temperature distribution for an initially spherical vapour bubble entering subcooled water: (*a*) 0 ms; (*b*) 3 ms; (*c*) 6 ms; (*d*) 9 ms; (*e*) 12 ms; (*f*) 15 ms; (*g*) 18.36 ms. The initial radius is 1 mm, translation velocity is 0.127 m s^{-1}, the ambient pressure is 1 atm, and the temperature difference is 3.35 K; t_c calculated from (2.2) is 46.2 ms. The circular arc in the lower border of the last frame marks the boundary of the computational domain.

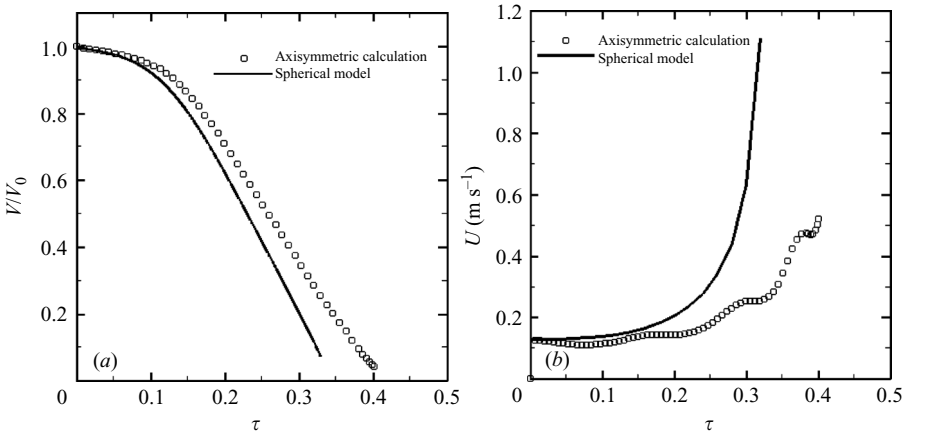


FIGURE 15. Comparison of (*a*) volume and (*b*) velocity with the spherical model (solid lines) for the same example as in figure 14; here $\tau = t/t_c$, with $t_c = 46.2$ ms, as defined in (2.2).

https://doi.org/10.1017/S0022112008000670 Published online by Cambridge University Press

to obtain convergence of the results over most of the evolution of the process, except perhaps in the very last stages of the collapse. Figure 15 shows a comparison between the current simulation and the spherical model. From figure 15(*a*), the collapse rate of the current calculation is only slightly slower than that of the spherical model, a result due to the slower translating velocity as shown in figure 15(*b*). Oscillations of the velocity in figure 15(*b*) indicate strong shape oscillations.

8.2. *Thick superheated liquid region*

The converse problem, that of an initially spherical vapour bubble encountering a superheated liquid, was also calculated. All the conditions are the same as in the the previous case except that now the liquid is superheated by 3.35 K.

It is well known that growth has a stabilizing effect on the spherical shape of a bubble because of the stretching of the surface produced by the divergence of the streamlines (see e.g. Plesset & Prosperetti 1977; Prosperetti & Hao 1999). Furthermore, the temperature boundary layer is stretched by the growth and the increasing added mass decreases the bubble translational velocity. All these factors produce an almost spherical bubble as can be seen in figure 16, which also shows the temperature distribution at different instants.

In the last three panels, the bubble is nearly stationary on the interface. One might say that, while a colder liquid 'attracts' a vapour bubble, a warmer one tends to 'repel' it. A similar tendency was found with the spherical model in Hao & Prosperetti (2000).

8.3. *Thin subcooled liquid region*

We now simulate the encounter of a bubble with a 'thin' region of subcooled liquid. The initial bubble radius is 0.5 mm, the initial velocity is $0.2\,\mathrm{m\,s^{-1}}$, and the water layer is subcooled by 3.35 K with a thickness of 0.5 mm. These conditions correspond to $t_c = 11.6$ ms, $Pe = 1173$ and $We = 0.324$. To mitigate the temperature wiggles mentioned before, in this case the transition between the two temperatures was smoothed quadratically over a thickness of 5 % of the layer thickness similarly to Hao & Prosperetti (2000).

Figure 17 shows the instantaneous temperature distribution. As it collapses, the bubble velocity increases as found before, with the effect that the residence time in the colder liquid is significantly reduced. Figure 18(*a*) shows the evolution of the bubble volume; the bubble is seen to lose about 80% of its initial volume as a consequence of its encounter with the subcooled layer. Figure 18(*b*) shows the time history of the bubble translation velocity, which is approximately doubled after passing through the layer.

8.4. *Thin superheated liquid region*

For a vapour bubble passing through a superheated liquid layer, arguments similar to those of § 8.2 can be applied, and the bubble maintains a nearly spherical shape.

Figure 19 shows the instantaneous temperature distribution for the same situation as in § 8.3, the only difference being that the liquid in the layer is now superheated by 3.35 K. Figure 20(*a*) illustrates the evolution of the volume. As shown in the figure, the bubble gains about 300 % of its volume. Figure 20(*b*) shows the time history of the bubble translation velocity, which decreases so much that the bubble appears to be nearly stationary at the end of the calculation.

https://doi.org/10.1017/S0022112008000670 Published online by Cambridge University Press

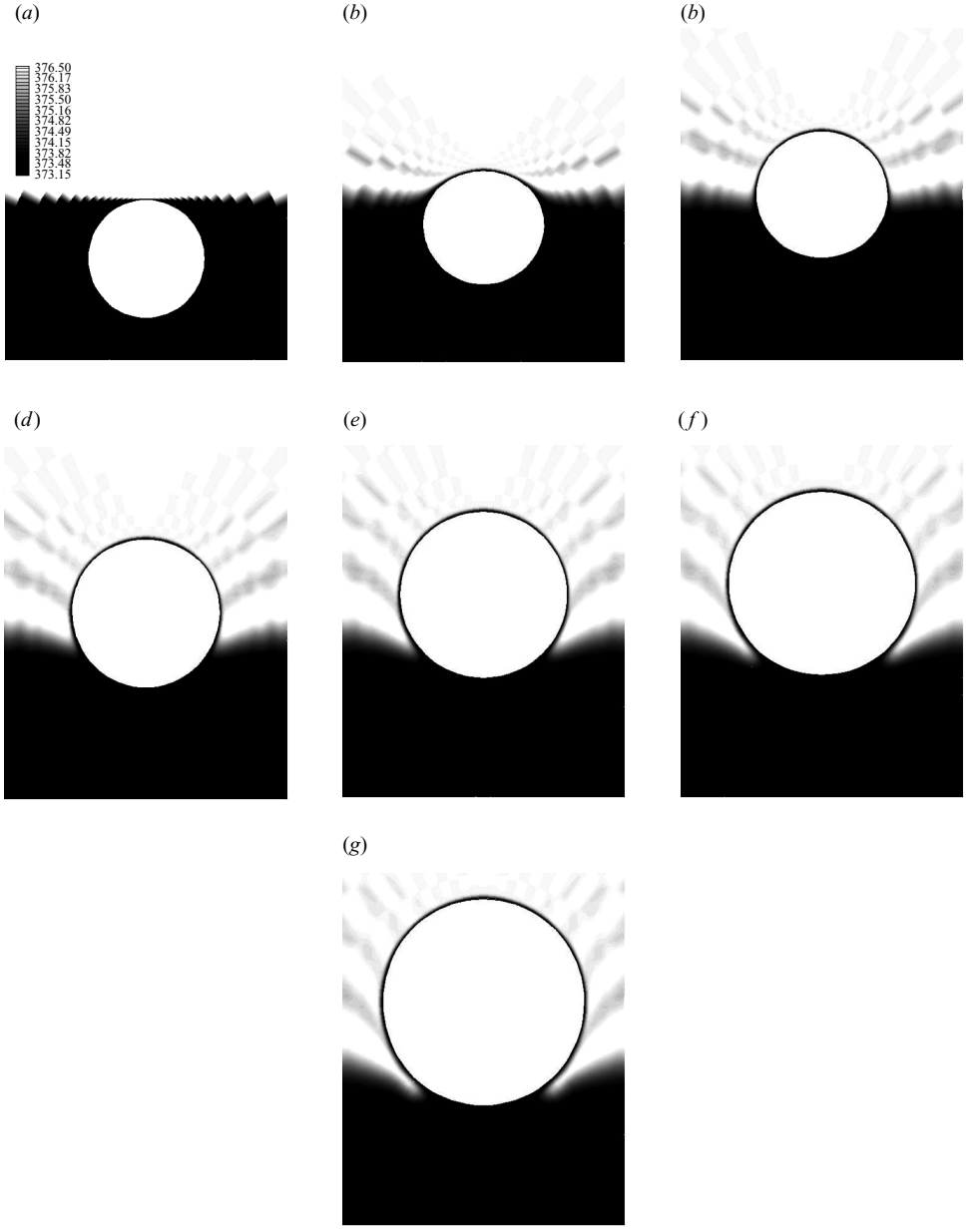


FIGURE 16. Instantaneous temperature distribution for an initially spherical vapour bubble entering superheated water: (*a*) 0 ms; (*b*) 5 ms; (*c*) 10 ms; (*d*) 15 ms; (*e*) 20 ms; (*f*) 25 ms; (*g*) 30 ms. The initial radius is 1 mm, translation velocity is 0.127 m s^{-1}, the ambient pressure is 1 atm and the temperature difference is 3.35 K; t_c calculated from (2.2) is 46.2 ms.

9. Conclusions

The behaviour of a vapour bubble in a subcooled or superheated liquid is the result of a complex interplay of fluid mechanics and heat transfer. The latter dictates the rate of change of the bubble volume by vapour condensation or generation. These volume changes strongly affect the bubble impulse and shape and, therefore,

https://doi.org/10.1017/S0022112008000670 Published online by Cambridge University Press

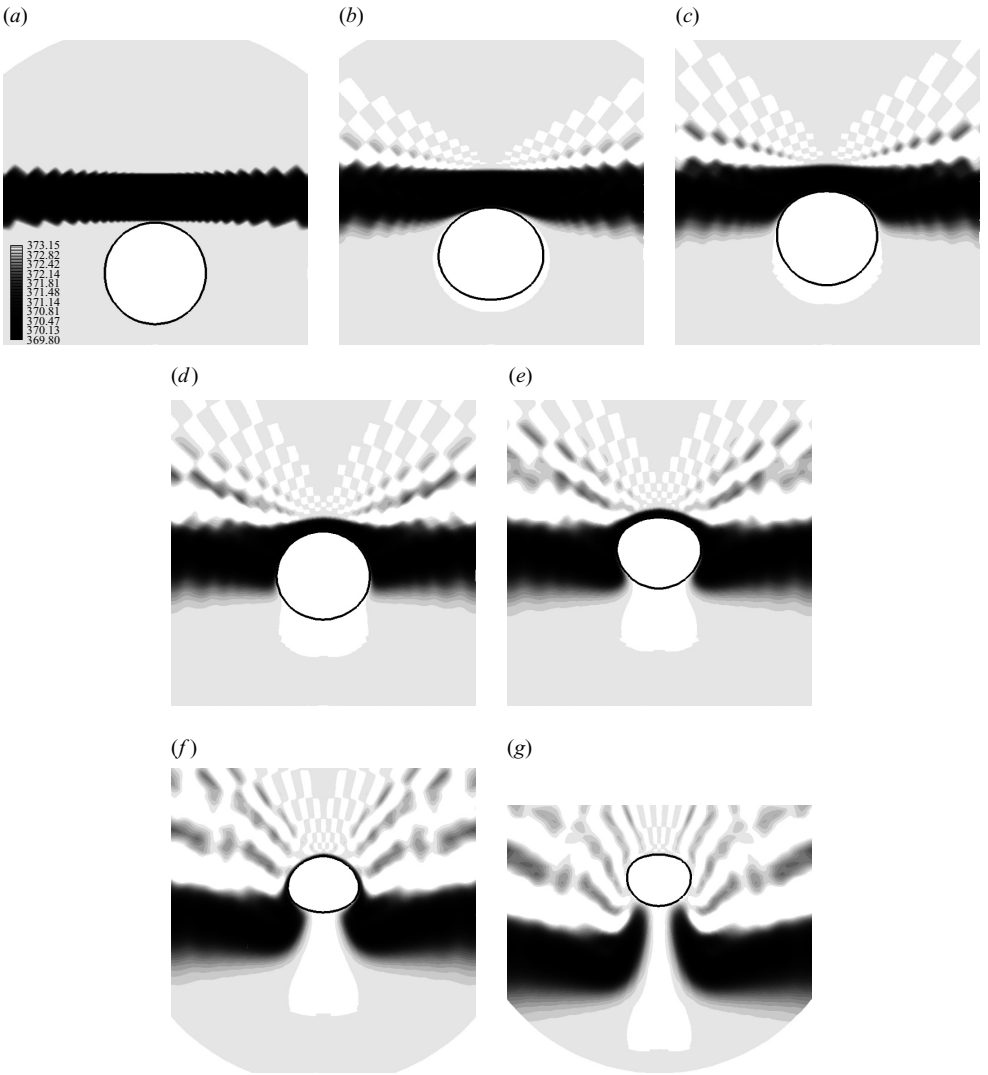


FIGURE 17. Instantaneous temperature distribution for the collapse of an initially spherical vapour bubble passing through a subcooled liquid layer: (*a*) 0 ms; (*b*) 1 ms; (*c*) 2 ms; (*d*) 3 ms; (*e*) 4 ms; (*f*) 4.889 ms; (*g*) 5.888 ms. The initial radius is 0.5 mm, velocity is 0.2 m s^{-1}, the ambient pressure is 1 atm and the water layer is subcooled by 3.35 K with a thickness of 0.5 mm. The corresponding $t_c = 11.6$ ms calculated from (2.2).

its velocity, which, in turn, influences the convective heat transfer. In this paper we have carried out numerical simulations allowing the bubble to deform and we have compared the results with those of simplified models. One of these models assumes the bubble to remain spherical, while the convective heat transfer is calculated with the assumption of a potential velocity field. The other model allows the bubble to deform into an oblate ellipsoid, but uses an empirical Nusselt number relation to estimate the heat transfer. While both models may give a reasonable estimate of the bubble collapse time in a subcooled liquid, we find that the details of the process are not well represented by either one of them.

https://doi.org/10.1017/S0022112008000670 Published online by Cambridge University Press

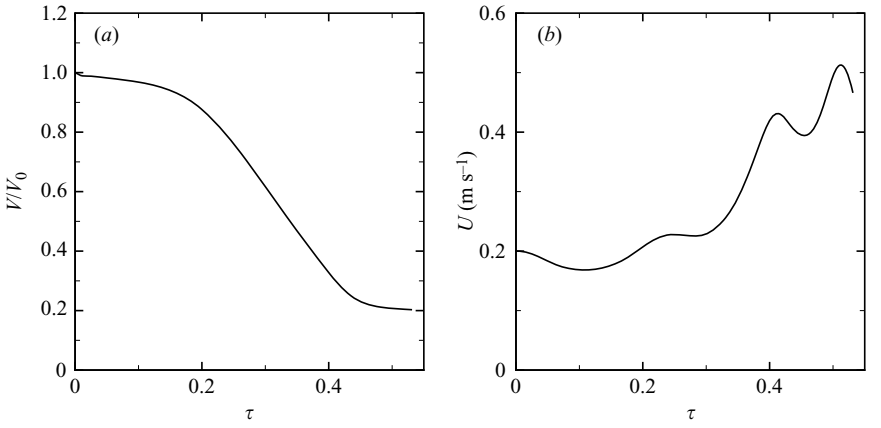


FIGURE 18. Evolution of (*a*) volume and (*b*) velocity for the same case as in figure 17. Here $\tau = t/t_c$, with $t_c = 11.6$ ms, as defined in (2.2).

In addition to a bubble placed in a liquid with a uniform temperature, we have also considered the interaction of bubbles with liquid regions at a different temperature. A bubble entering a subcooled region rapidly condenses and, as a consequence, it penetrates the colder liquid with an increasing velocity. Even if the subcooled region is thin, the loss of volume is substantial. Conversely, a bubble encountering a superheated liquid grows and slows down. It may be said that cooler liquid regions 'attract' vapour bubbles, while warmer ones 'repel' them.

This study has been supported by NASA under grant NNC05GA47G.

Appendix A. Derivation of (3.6)

With the assumption of a spatially uniform pressure inside the bubble, the equation for the conservation of enthalpy may be written as

$$\frac{\partial}{\partial t}(\rho_v h_v) + \nabla\cdot(\rho_v h_v \boldsymbol{u}_v + \boldsymbol{q}_v) = \dot{p}_v \tag{A 1}$$

where $\boldsymbol{q}_v$ is the heat flux and $\dot{p}_v = \mathrm{d}p_v/\mathrm{d}t$. Here and throughout this appendix vapour quantities are designated by the subscript v; liquid quantities carry no subscript. For a perfect gas, $\rho_v h_v = \gamma p_v/(\gamma-1)$, where γ is the ratio of specific heats. Upon integrating over the bubble volume we thus find

$$\frac{V}{\gamma-1}\dot{p}_v + \frac{\gamma}{\gamma-1}p_v \oint_S \boldsymbol{u}_v\cdot\boldsymbol{n}\,\mathrm{d}S = -\oint_S \boldsymbol{q}_v\cdot\boldsymbol{n}\,\mathrm{d}S \tag{A 2}$$

Conservation of energy at the interface is expressed by

$$(\boldsymbol{q}-\boldsymbol{q}_v)\cdot\boldsymbol{n} = L\rho_v(\boldsymbol{u}_v-\boldsymbol{v})\cdot\boldsymbol{n}, \tag{A 3}$$

which, integrated over the interface where, as discussed in § 3, the temperature T_s is uniform and, therefore, the vapour density ρ_v is constant, gives

$$\begin{aligned}\oint_S \boldsymbol{u}_v\cdot\boldsymbol{n}\,\mathrm{d}S &= \oint_S \boldsymbol{v}\cdot\boldsymbol{n}\,\mathrm{d}S + \frac{1}{\rho_v L}\oint(\boldsymbol{q}-\boldsymbol{q}_v)\cdot\boldsymbol{n}\,\mathrm{d}S \\ &= \dot{V} + \frac{1}{\rho_v L}\oint(\boldsymbol{q}-\boldsymbol{q}_v)\cdot\boldsymbol{n}\,\mathrm{d}S\end{aligned} \tag{A 4}$$

https://doi.org/10.1017/S0022112008000670 Published online by Cambridge University Press

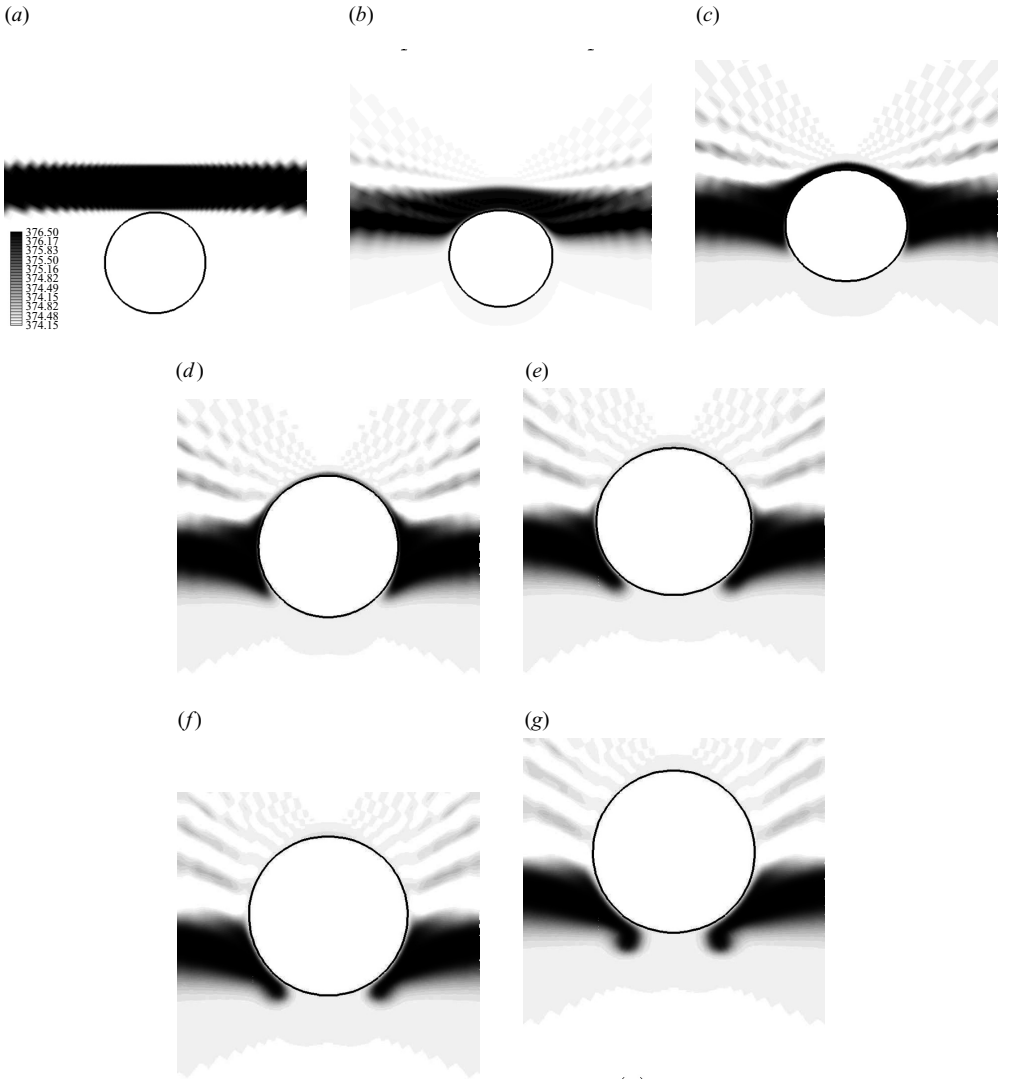


FIGURE 19. Instantaneous temperature distribution for the growth of an initially spherical vapour bubble travelling through a superheated liquid layer: (*a*) 0 ms; (*b*) 2 ms; (*c*) 4 ms; (*d*) 6 ms; (*e*) 8 ms; (*f*) 10 ms; (*g*) 12 ms. The initial radius is 0.5 mm, velocity is 0.2 m s^{-1}, the ambient pressure is 1 atm and the hot water layer is superheated by 3.35 K with a thickness of 0.5 mm, corresponding to $t_c = 11.6$, $Pe = 1173$ and $We = 0.324$.

Upon substituting into (A 2) and rearranging we have

$$\oint_S \boldsymbol{q}\cdot\boldsymbol{n}\,\mathrm{d}S = \frac{c_s}{c_{pv}}\oint_S \boldsymbol{q}_v\cdot\boldsymbol{n}\,\mathrm{d}S - \frac{L}{(\gamma-1)c_{pv}T_v}(V\dot{p}_v + \gamma p_v\dot{V}) \tag{A 5}$$

When the characteristic time scale for surface temperature variation is long compared with the diffusion time in the vapour, the vapour is nearly isothermal. Under this hypothesis, the energy equation in the vapour can be approximated as

$$\rho_v c_{pv}\dot{T}_s - \dot{p}_v \simeq -\nabla\cdot\boldsymbol{q}_v. \tag{A 6}$$

https://doi.org/10.1017/S0022112008000670 Published online by Cambridge University Press

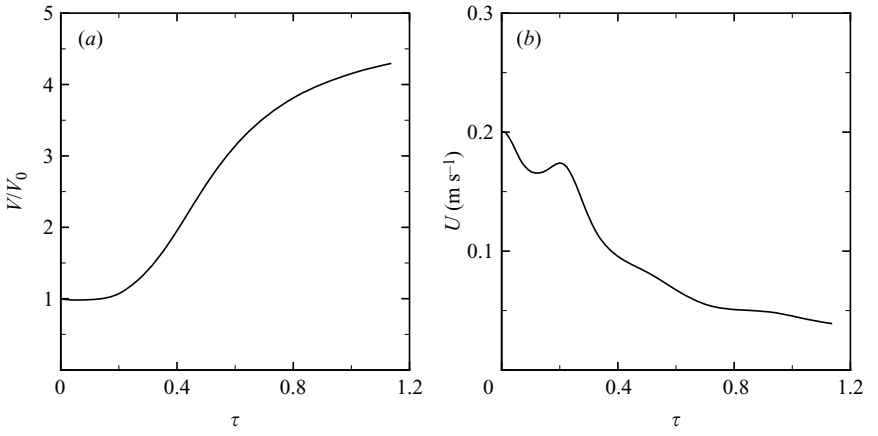


FIGURE 20. Evolution of (*a*) volume and (*b*) velocity for the same case in figure 19. Here $\tau = t/t_c$, with $t_c = 11.6$ ms, as defined in (2.2).

A formal derivation of this result for a spherical bubble can be found in Hao & Prosperetti (1999). Upon integrating over the bubble volume we have

$$\oint \boldsymbol{n}\cdot\boldsymbol{q}_v \,\mathrm{d}S \simeq -V\left(\frac{\gamma}{\gamma-1}\frac{p}{T_s}\dot{T}_s - \dot{p}\right), \tag{A 7}$$

which, upon substitution into (A 5), gives (3.6).

REFERENCES

ABDELMESSIH, A. H., HOOPER, F. C. & NANGIA, S. 1972 Flow effects on bubble growth and collapse in surface boiling. *Intl J. Heat Mass Transfer* **15**, 115–125.

BLANCO, A. & MAGNAUDET, J. 1995 The structure of axisymmetric high-Reynolds number flow around an ellipsoidal bubble of fixed shape. *Phys. Fluids* **7**, 1265–1274.

BROWN, D. L., CORTEZ, R. & MINION, M. L. 2001 Accurate projection methods for the incompressible Navier-Stokes equations. *J. Comput. Phys.* **168**, 464–499.

CAO, J. & CHRISTENSEN, R. N. 2000 Analysis of moving boundary problem for bubble collapse in binary solutions. *Num. Heat Transfer* A **87**, 681–699.

CHEN, Y. & MAYINGER, F. 1992 Measurement of heat transfer at the phase interface of condensing bubbles. *Intl J. Multiphase Flow* **18**, 877–890.

DARWIN, C. 1953 Note on hydrodynamics. *Proc. Camb. Phil. Soc.* **49**, 342–354.

DURAISWAMI, R. & PROSPERETTI, A. 1992 Orthogonal mapping in two dimensions. *J. Comput. Phys.* **98**, 254–268.

EAMES, I., BELCHER, S. E. & HUNT, J. C. R. 1994 Drift, partial drift and Darwin's proposition. *J. Fluid Mech.* **275**, 201–223.

FLORSCHUETZ, L. & CHAO, B. 1965 On the mechanics of vapour bubble collapse. *J. Heat Transfer* **87**, 209–220.

FRANCOIS, M. & SHYY, W. 2003 Computations of drop dynamics with the immersed boundary method, Part 1: Numerical algorithm and buoyancy-induced effect. *Numer. Heat Transfer* B **44**, 101–118.

GUMEROV, N. 1996 The heat and mass transfer of a vapour bubble with translatory motion at high Nusselt numbers. *Intl J. Multiphase Flow* **22**, 259–272.

HAO, Y. & PROSPERETTI, A. 1999 The dynamics of vapour bubbles in acoustic pressure fields. *Phys. Fluids* **11**, 2008–2019.

HAO, Y. & PROSPERETTI, A. 2000 The collapse of vapour bubbles in a spatially non-uniform flow. *Intl J. Heat Mass Transfer* **43**, 3539–3550.

https://doi.org/10.1017/S0022112008000670 Published online by Cambridge University Press

Hashimoto, H. & Kawano, S. 1990 A study on encapsulated liquid drop formation in liquid-liquid-gas systems. *JSME Intl J.* **B33**, 729–735.

Ivashnyov, O. E. & Smirnov, N. N. 2004 Thermal growth of a vapour bubble moving in superheated liquid. *Phys. Fluids* **16**, 809–823.

Kalman, H. & Ullmann, A. 1999 Experimental analysis of bubble shapes during condensation in miscible and immiscible liquids. *J. Heat Transfer* **121**, 496–502.

Kawano, S., Hashimoto, H. & Ihara, A. 1996 Sequential production of mm-sized spherical shells in liquid-liquid gas systems. *Trans. ASME: J. Fluids Engng* **118**, 614–618.

Labuntsov, D. & Kryukov, A. 1979 Analysis of intensive evaporation and condensation. *Intl J. Heat Mass Transfer* **22**, 989–1002.

Leal, L. G. 1989 Velocity transport and wake structure for bluff bodies at finite Reynolds number. *Phys. Fluids* A **1**, 124–131.

Legendre, D., Borée, J. & Magnaudet, J. 1998 Thermal and dynamic evolution of a spherical bubble moving steadily in a superheated or subcooled liquid. *Phys. Fluids* **10**, 1256–1272.

Levich, V. 1962 *Physicochemical Hydrodynamics*. Prentice-Hall.

Li, W. Z. & Yan, Y. Y. 2002 An alternating dependent variables (ADV) method for treating slip boundary conditions of free sutface flows with heat and mass transfer. *Numer. Heat Transfer* B **41**, 165–189.

Li, W. Z., Yan, Y. Y. & Hull, J. B. 2003*a* The propagation of temperature and concentration fields around a deformed gas bubble rising in a quiescent hot or bi-solution liquid. *Intl J. Numer. Meth. Heat Fluid Flow* **8**, 940–963.

Li, W. Z., Yan, Y. Y. & Smith, J. M. 2003*b* A numerical study of the interfacial transport characteristics outside spheroidal bubbles and solids. *Intl J. Multiphase Flow* **29**, 435–460.

Lighthill, M. J. 1956 Drift. *J. Fluid Mech.* **1**, 31–53, and corrigendum, **2**, 311–312.

Milne-Thomson, L. 1960 *Theoretical Hydrodynamics*, 4th edn. MacMillan.

Moalem, D. & Sideman, S. 1973 The effect of motion on bubble collapse. *Intl J. Heat Mass Transfer* **16**, 2321–2329.

Moore, D. 1965 The velocity of rise of distorted gas bubbles in a liquid of small viscosity. *J. Fluid Mech.* **23**, 749–766.

Mukherjee, A. & Dhir, V. 2004 Study of lateral merger of vapour bubbles during nucleate pool boiling. *J. Heat Transfer* **126**, 1023–1039.

Osher, S. & Fedkiw, R. 2001 Level set methods: an overview and some recent results. *J. Comput. Phys.* **169**, 463–502.

Plesset, M. & Prosperetti, A. 1977 Bubble dynamics and cavitation. *Annu. Rev. Fluid Mech.* **9**, 145–185.

Prosperetti, A. & Hao, Y. 1999 Modelling of spherical gas bubble oscillations and sonoluminescence. *Phil. Trans. R. Soc. Lond.* A **357**, 203–223.

Prosperetti, A. & Hao, Y. 2002 Vapour bubbles in flow and acoustic fields. *Ann. New York Acad. Sci.* **974**, 328–347.

Raad, P. E. & R., B. 2005 The three-dimensional Eulerian-Lagrangian marker and micro cell method for the simulation of free surface flows. *J. Comput. Phys.* **203**, 668–699.

Ruckenstein, E. 1959 On heat transfer between vapour bubbles in motion and the boiling liquid from which they are generated. *Chem. Engng Sci.* **10**, 22–30.

Ruckenstein, E. & Davis, J. 1971 The effects of bubble translation on vapour bubble growth in a superheated liquid. *Intl J. Heat Mass Transfer* **14**, 939–952.

Ryskin, G. & Leal, L. 1983 Orthogonal mapping in two dimensions. *J. Comput. Phys.* **98**, 254–268.

Ryskin, G. & Leal, L. 1984 Numerical solution of free-boundary problems in fluid mechanics. Part 5. Buoyancy-driven motion of a gas bubble through a quiescent liquid. *J. Fluid Mech.* **148**, 19–35.

Sardić-Mitrović, A. N., Mohamed, N. A. & Fernando, H. J. S. 1999 Gravitational settling of particles through density interfaces. *J. Fluid Mech.* **381**, 175–198.

Scardovelli, R. & Zaleski, S. 1999 Direct numerical simulation of free-surface and interfacial flow. *Annu. Rev. Fluid Dyn.* **31**, 567–603.

Scardovelli, R. & Zaleski, S. 2003 Interface reconstruction with least-square fit and split Eulerian-Lagrangian advection. *Intl J. Numer. Meth. Fluids* **41**, 251–274.

Shirani, E., Ashgriz, N. & Mostaghimi, J. 2005 Interface pressure calculation based on conservation of momentum for front capturing methods. *J. Comput. Phys.* **203**, 154–175.

https://doi.org/10.1017/S0022112008000670 Published online by Cambridge University Press

Son, G. & Dhir, V. 1997 Numerical simulation of saturated film boiling on a horizontal surface. *J. Heat Transfer* **119**, 525–533.

Son, G., Ramanujapu, N. & Dhir, V. 2002 Numerical simulation of bubble merger process on a single nucleation site during pool nucleate boiling. *J. Heat Transfer* **124**, 51–62.

Szeri, A. J., Storey, B. D., Pearson, A. & Blake, J. R. 2003 Heat and mass transfer during the violent collapse of nonspherical bubbles. *Phys. Fluids* **15**, 2576–2586.

Takagi, S., Matsumoto, Y. & Huang, H. 1997 Numerical analysis of a single rising bubble using boundary-fitted coordinate system. *JSME Intl J.* **B40**, 42–50.

Udaykumar, H. S., Mittal, R., Rampunggoon, P. & Khanna, A. 2001 A sharp interface Cartesian grid method for simulating flows with complex moving boundaries. *J. Comput. Phys.* **174**, 345–380.

Wittke, D. & Chao, B. 1967 Collapse of vapour bubbles with translatory motion. *J. Heat Transfer* **89**, 17–24.

Yang, B. & Prosperetti, A. 2006 A second-order boundary-fitted projection method for free-surface flow computations. *J. Comput. Phys.* **213**, 574–590.

Yang, B. & Prosperetti, A. 2007 Linear stability of the flow past a spheroidal bubble. *J. Fluid Mech.* **582**, 53–78.

Yang, B., Prosperetti, A. & Takagi, S. 2003 The transient rise of a bubble subject to shape or volume changes. *Phys. Fluids* **15**, 2640–2648.

Ye, T., Shyy, W. & Chung, J. N. 2003 A fixed-grid, sharp-interface method for bubble dynamics and phase change. *J. Comput. Phys.* **174**, 781–815.

Yuan, H. & Prosperetti, A. 1997 Gas-liquid heat transfer in a bubble collapsing near a wall. *Phys. Fluids* **9**, 127–142.

https://doi.org/10.1017/S0022112008000670 Published online by Cambridge University Press